Adv. Opt. Techn., Vol. 1 (2012), pp. 151–169 • Copyright © 2012 THOSS Media and De Gruyter. DOI 10.1515/aot-2012-0014

Review Article

Fresnel incoherent correlation holography (FINCH): a review of research

Joseph Rosen[1,*] and Gary Brooker[2]

[1] Department of Electrical and Computer Engineering, Ben-Gurion University of the Negev, P.O. Box 653, Beer-Sheva 84105, Israel

[2] Department of Biomedical Engineering and Microscopy Center, Montgomery County Campus, Johns Hopkins University, 9605 Medical Center Drive Suite 240, Rockville, MD 20850, USA

* Corresponding author
e-mail: rosen@ee.bgu.ac.il
Received April 2, 2012; accepted June 4, 2012

Abstract

In this review, we describe our method for creating holograms of incoherent objects, dubbed Fresnel incoherent correlation holography (FINCH). FINCH creates holograms by a single-channel on-axis incoherent interferometer process. Like any Fresnel hologram, the object is correlated with quadratic phase functions, but the correlation is carried out without any movement. Generally, in the FINCH system, light is reflected, or emitted, from a three-dimensional (3D) object, propagates through a spatial light modulator (SLM), and is recorded by a digital camera. The SLM is used as a beam-splitter of the single-channel incoherent interferometer, such that each spherical beam originated from each object point is split into two spherical beams with two different curve radiuses. Incoherent summing of the entire interferences between all the couples of the spherical beams creates the Fresnel hologram of the observed 3D object. When this hologram is reconstructed in the computer, the 3D properties of the object are revealed. In this review, we describe various aspects of FINCH which have been described recently, including FINCH of reflected white light, FINCH of fluorescence objects, a FINCH-based holographic fluorescence microscope, a FINCH configuration which capitalizes on the polarization sensitivity of the SLM and finally FINCH is analyzed in view of linear system theory.

Keywords: diffraction gratings; diffractive optics; digital holography; fluorescence microscopy; three-dimensional image acquisition.

1. Introduction

Holographic imaging offers a reliable and fast method to capture the complete three-dimensional (3D) information of the scene from a single perspective. However, holography is not widely applied to the regime of white light imaging, because white light is incoherent and, in general, creating holograms requires a coherent interferometer system. In this review, we describe our recently invented method of acquiring incoherent digital holograms. The term incoherent digital hologram means that incoherent light beams reflected or emitted from real existing objects interfere with each other. The resulting interferogram is recorded by a digital camera and digitally processed to yield a hologram. This hologram is reconstructed in the computer so that 3D images appear on the computer's screen. The coherent optical recording of a classical holographic system is not applicable to incoherent objects because interference between reference and object incoherent beams cannot occur. Therefore, different holographic acquisition methods should be employed for generating an incoherent digital hologram.

The oldest methods of recording incoherent holograms have made use of the property that every incoherent object is composed of many source points, each of which is self-spatial coherent and therefore can create an interference pattern with light coming from the point's mirrored image. Under this general principle, there are various types of holograms, including Fourier [1, 2] and Fresnel holograms [3–7]. The process of beam interfering demands high levels of light intensity, extreme stability of the optical setup, and a relatively narrow bandwidth light source. These limitations have prevented holograms from becoming widely used for many practical applications. More recently, several groups of researchers have proposed computing holograms of 3D incoherently illuminated objects from a set of images taken from different points of view [8–11]. This method, although it shows promising prospects, is relatively slow because it is based on capturing tens of scene images from different view angles. Another method is called scanning holography [12–16] in which a pattern of interference between two spherical waves scans the object such that at each and every scanning position, the light intensity is integrated by a point detector. The overall process yields a Fresnel hologram obtained as a correlation between the object and the interference pattern.

Our recently proposed incoherent digital hologram method is dubbed Fresnel incoherent correlation holography (FINCH) which can refer to the method of producing a hologram or the resultant hologram [17]. FINCH is actually based on a single-channel on-axis incoherent interferometer. Like any Fresnel holography, in FINCH the object is correlated with quadratic phase functions, but the correlation is carried out without any movement and without multiplexing the image of the scene. This article reviews the latest developments of FINCH of reflected white light [17], FINCH of fluorescence objects [18], a FINCH-based holographic fluorescence microscope

[19–21], and finally FINCH operating with two multiplexed diffractive lenses [22].

2. General properties of Fresnel holograms

The type of hologram discussed in this review is the digital Fresnel hologram. To understand the operation principle of any general Fresnel hologram, let us look at the difference between regular and Fresnel-holographic imaging systems. In classical imaging, image formation of objects at different distances from the lens results in a sharp image at the image plane for objects at only one position from the lens. The other objects at different distances from the lens are out of focus. The FINCH system, by contrast, projects a set of rings onto the plane of the image for each and every point at every plane of the object being viewed. The depth of the points is encoded by the density of the rings such that points which are closer to the system project denser rings than distant points. Because of this encoding method, the 3D information in the volume being imaged is recorded by the recording medium. Therefore, each plane in the image space reconstructed from a Fresnel hologram is in focus at a different axial distance. The encoding is accomplished by the presence of one of the holographic systems in the image path. Each holographic system, coherent or incoherent, has a different method to project the ring structure on the detector plane. At this point it should be noted that this graphical description of projecting rings by every object's point actually expresses the mathematical two-dimensional (2D) correlation (or convolution) between the object function and a quadratic phase function. In other words, the methods of creating Fresnel holograms are different from each other by the way they spatially correlate the quadratic phase function with the 3D scene. Another issue to note is that the correlation should be done with a quadratic phase function that is somehow 'sensitive' to the axial locations of the object points. Otherwise, these locations are not encoded into the hologram. The systems described in this review satisfy the condition that the quadratic phase function is dependent on the axial distance of each and every object point. This means that indeed points, which are far from the system, project a quadratic phase function with fewer cycles per radial length than nearby points, and by this condition the holograms can actually image the 3D scene properly.

The Fresnel hologram of a point is a sum of at least three main functions, a constant bias, a quadratic phase function, and its complex conjugate. The object function is actually correlated with all three functions. However, the useful information, with which the holographic imaging is realized, is the correlation with just one of the two quadratic phase functions. The correlation with the other quadratic phase function induces the well-known twin image [23]. This means that the detected signal in the holographic system contains three superposed correlation functions, whereas only one of them is the required correlation between the object and the quadratic phase function. Therefore, the digital processing of the detected signal should have the ability to eliminate the two unnecessary terms.

The definition of a Fresnel hologram is any hologram that contains, at least, a correlation (or convolution) between an object function and a quadratic phase function. Moreover, the quadratic phase function must be parameterized according to the axial distance of the object points from the detection plane. In other words, the number of cycles per radial distance of each quadratic phase function in the correlation is dependent on the z distance of each object point. Formally, a hologram is called a Fresnel hologram if its distribution function contains the following term:

$$H(u,v)=\iiint g(x,y,z)\exp\left\{i\frac{2\pi\beta}{z}\left[(u-x)^2+(v-y)^2\right]\right\}dxdydz, \quad (1)$$

where $g(x,y,z)$ is the 3D object function and β is a constant. Indeed, in Eq. (1) the phase of the exponent is dependent on z, the axial location of the object. In case the object is illuminated by a coherent wave, $H(u,v)$ given by Eq. (1) is the complex amplitude of the coherent electromagnetic field directly obtained, under the paraxial approximation [23], by a free space propagation from the object to the detection plane. However, we deal here with incoherent illumination, for which alternative methods to the free propagation should be applied. In fact, in this review we describe such a method to obtain the desired correlation with the quadratic phase function given in Eq. (1), and this method indeed operates under incoherent illumination.

3. Fresnel incoherent correlation holography (FINCH) for reflected white light

The first FINCH system [17] is shown in Figure 1. A white light source illuminates a 3D object, and the reflected light from the object is captured by a digital camera after passing through a lens L and a spatial light modulator (SLM). As is common in such cases, we analyze the system by following its response to an input object of a single infinitesimal point. Knowing the system's point spread function (PSF) enables one to realize the system operation for any general object.

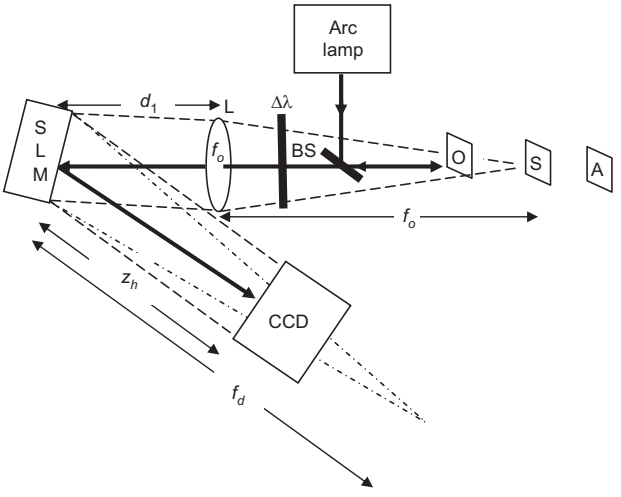

Figure 1 Schematic of FINCH recorder. BS, beam splitter; SLM, spatial light modulator; CCD, charge-coupled device; L is a spherical lens with f_o=25 cm focal length. Δλ indicates a chromatic filter with a bandwidth of Δλ=60 nm.

Analysis of a beam originated from a narrowband infinitesimal point source is done using Fresnel diffraction theory [23], because such a source is spatially coherent by definition.

A Fresnel hologram of a point object is obtained when the two interfering beams are, for instance, plane and spherical beams. Such a goal is achieved if the SLM's reflection function $R(x,y)$ is of the form:

$$R(x,y)=\frac{1}{2}+\frac{1}{2}\exp\left[-\frac{i\pi}{\lambda f_d}(x^2+y^2)+i\theta\right]=\frac{1}{2}+\frac{1}{2}\mathrm{Q}\left(-\frac{1}{f_d}\right)\exp(i\theta), \quad (2)$$

where f_d is the focal length of the diffractive lens displayed on the SLM. For the sake of shortening, the quadratic phase function is designated by the function Q, such that $\mathrm{Q}(b)=\exp[(i\pi b/\lambda)(x^2+y^2)]$. When a plane wave hits the SLM, the first constant term 1/2 in Eq. (2) represents the reflected plane wave, and the quadratic phase term is responsible for the reflected spherical wave in the paraxial approximation. The angle θ plays an important role later in the computation process to eliminate the twin image and the bias term.

A point source located at the point (x_s,y_s,z_s) a distance z_s from a spherical positive lens, with f_o focal length, induces on the lens plane a diverging spherical wave of the form of $C_1(\overline{r}_s)Q(1/z_s)L(-\overline{r}_s/z_s)$, where the function L stands for a linear phase function, such that $L(\overline{s})=\exp\left[i2\pi\lambda^{-1}(s_x x+s_y y)\right]$, $\overline{r}_s=(x_s,y_s)$ and $C_1(\overline{r}_s)$is a complex constant dependent on the source point's location. On the digital camera plane at a distance z_h from the SLM, the intensity of the recorded hologram is:

$$\begin{aligned} I_P(x,y)&=\left|C_1(\overline{r}_s)L\left(\frac{-\overline{r}_s}{z_s}\right)Q\left(\frac{1}{z_s}\right)Q\left(\frac{-1}{f_o}\right)*Q\left(\frac{1}{d_1}\right)\right. \\ &\left.\left[\frac{1}{2}+\frac{1}{2}\exp(i\theta)Q\left(\frac{-1}{f_d}\right)\right]*Q\left(\frac{1}{z_h}\right)\right|^2 \\ &=\left|C_2(\overline{r}_s)L\left(\frac{-\overline{r}_s f_e}{z_s(f_e+d_1)}\right)Q\left(\frac{1}{f_e+d_1}\right)\right. \\ &\left.\left[\frac{1}{2}+\frac{1}{2}\exp(i\theta)Q\left(\frac{-1}{f_d}\right)\right]*Q\left(\frac{1}{z_h}\right)\right|^2, \end{aligned} \quad (3)$$

where the asterisk denotes 2D convolution. The explanation of Eq. (3) is as follows: the three left-most terms $C_1(\overline{r}_s)L(-\overline{r}_s/z_s)Q(1/z_s)$ describe the point source wave as is seen from the plane of lens L. This wave is multiplied by the lens L [multiplied by $Q(-1/f_o)$], propagates a distance d_1 [convolved with $Q(1/d_1)$] and meets the SLM where its transparency is in the square brackets of Eq. (3). Beyond the SLM there are two different beams propagating an additional distance z_h until the camera [convolved with $Q(1/z_h)$]. Finally, the magnitude of the interference is squared to yield the intensity distribution of the recoded hologram. The result of $I_P(x,y)$, after calculating the square magnitude in Eq. (3), is the PSF for any source point located at any point (x_s,y_s,z_s) on the object space of the FINCH, as follows:

$$\begin{aligned} I_P(x,y)=A_o\left(2+\exp\left\{\frac{i\pi}{\lambda z_r}\left[\left(x-\frac{z_h f_e x_s}{z_s(f_e+d_1)}\right)^2\right.\right.\right. \\ \left.+\left(y-\frac{z_h f_e y_s}{z_s(f_e+d_1)}\right)^2\right]+i\theta\Big\} \\ +\exp\left\{\frac{-i\pi}{\lambda z_r}\left[\left(x-\frac{z_h f_e x_s}{z_s(f_e+d_1)}\right)^2\right.\right. \\ \left.\left.\left.+\left(y-\frac{z_h f_e y_s}{z_s(f_e+d_1)}\right)^2\right]-i\theta\right\}\right), \end{aligned} \quad (4)$$

where A_o is a constant and z_r, the reconstruction distance of the object point, is given by:

$$z_r=\pm\frac{(f_1+z_h)(f_e+d_1+z_h)}{f_1-f_e-d_1},$$
$$\text{where } f_1=\frac{f_d(f_e+d_1)}{f_d-(f_e+d_1)} \quad \text{and} \quad f_e=\frac{z_s f_o}{(f_o-z_s)} \quad (5)$$

The transverse location of the reconstructed object point is:

$$\overline{r}_r=\overline{r}_s\frac{z_h f_e}{z_s(f_e+d_1)}, \text{ where } \overline{r}_r=(x_r,y_r) \quad (6)$$

The sign '±' in Eq. (5) indicates the possibility to reconstruct from the hologram either the virtual or the real image respectively, depending upon whether the first or second exponential term is chosen from Eq. (4).

It is easy to see by calculating Eq. (3), that as long as the source point is located on the front focal plane of L, the interference occurs between a plane and a spherical (in the paraxial approximation) wave. For the special object plane of the front focal plane of the lens where $z_s=f_o$ the expressions in Eqs. (4) and (5) become simpler because for that plane $f_e\to\infty$ and therefore $f_1=-f_d$ and $z_r=\pm|f_d-z_h|$. The reconstruction distance of the point image from an equivalent optical hologram is z_r, although in the present case the hologram is of course digital, and the reconstruction is done by the computer. Eq. (4) is the expression of the transparency function of a hologram created by an object point and recorded by a FINCH system. This hologram has several unique properties. The transverse magnification M_T is expressed as $M_T=\partial x_r/\partial x_s=z_h/f_o$ for an object located on the front focal plane, and $M_T=f_e z_h/z_s(f_e+d_1)$ for any other plane.

For a general 3D object $g(x_s,y_s,z_s)$ illuminated by a narrowband incoherent illumination, the intensity of the recorded hologram is an integral of the entire PSF given by Eq. (4), over all the object intensity $g(x_s,y_s,z_s)$, as follows:

$$\begin{aligned} H(x,y)\cong A_o\left(C+\iiint g(x_s,y_s,z_s)\exp\left\{\frac{i\pi}{\lambda z_r}\left[(x-x_r)^2\right.\right.\right. \\ \left.\left.+(y-y_r)^2\right]+i\theta\right\}dx_s dy_s dz_s+\iiint g(x_s,y_s,z_s) \\ \left.\exp\left\{\frac{-i\pi}{\lambda z_r}\left[(x-x_r)^2+(y-y_r)^2\right]-i\theta\right\}dx_s dy_s dz_s\right). \end{aligned} \quad (7)$$

In addition to a constant term C, Eq. (7) contains two terms of correlation between an object and a quadratic phase function, z_s-dependent via z_r, which means that the recorded hologram is indeed a Fresnel hologram. To remain with a single correlation term out of the three terms given in Eq. (7), we follow the phase shifting procedure of on-axis digital holography [17]. Three holograms of the same object are recorded each of which with a different phase constant θ. The final hologram H_F is a superposition according to the following equation:

$$\begin{aligned} H_F(x,y) = & H_1(x,y)\left[\exp(\pm i\theta_3) - \exp(\pm i\theta_2)\right] \\ & + H_2(x,y)\left[\exp(\pm i\theta_1) - \exp(\pm i\theta_3)\right] \\ & + H_3(x,y)\left[\exp(\pm i\theta_2) - \exp(\pm i\theta_1)\right], \end{aligned} \tag{8}$$

where $H_i(x,y)$ is the i-th recorded hologram of the form of Eq. (7) and θ_i is the phase constant of the i-th SLM's quadratic phase used during the recording process. The choice between the signs in the exponents of Eq. (8) determines which image, virtual or real, is kept in the final hologram. A 3D image $g'(x,y,z)$ can be reconstructed from $H_F(x,y)$ by calculating the Fresnel propagation formula, as follows:

$$g'(x,y,z) = H_F(x,y) * \exp\left[\frac{\pm i\pi}{\lambda z_r}\left(x^2+y^2\right)\right], \tag{9}$$

The system shown in Figure 1 was used to record the three holograms [17]. The SLM (Holoeye HEO 1080P) is phase only and, thus, the desired function given by Eq. (2) cannot be directly displayed on this SLM. To overcome this obstacle, the phase function $Q(-1/f_d)$ is displayed randomly on only half of the SLM pixels. These pixels were represented in the second term of Eq. (2), whereas the rest of the pixels representing the first constant term in Eq. (2) were modulated with a constant phase. The randomness in distributing the two phase functions has been required because organized non-random structure produces unnecessary diffraction orders, and therefore results in lower interference efficiency. The pixels were divided equally, half to each diffractive element, to create two wavefronts with equal energy. By this method the SLM function becomes a good approximation to $R(x,y)$ of Eq. (2).

The SLM has 1920×1080 pixels in a display of 16.6×10.2 mm, where only the central 1024×1024 pixels were used for implementing the phase mask. The phase distribution of the three reflection masks displayed on the SLM, with phase constants of 0°, 120° and 240°, are shown in Figure 2A, B and C, respectively. The other specifications of the system of Figure 2 are: f_o=250 mm, f_d=430 mm, d_1=132 mm, z_h=260 mm.

Three white on black letters each of the size 2×2 mm were located at the vicinity of front focal point of the lens. 'O' was at z=-24 mm, 'S' was at z=-48 mm and 'A' was at z=-72 mm. These letters were illuminated by a mercury arc lamp. A filter which passed a Poisson-like power spectrum from 574 to 725 nm light with a peak wavelength of 599 nm and a bandwidth (full width at half-maximum) of 60 nm was positioned between the beam splitter and the lens L. The three holograms, each for a different phase constant of the SLM, were recorded by a digital camera and processed by the computer. The final hologram $H_F(x,y)$ was calculated according to Eq. (8) and its magnitude and phase distributions are depicted in Figure 2E and F, respectively.

The hologram $H_F(x,y)$ was reconstructed in the computer by calculating the Fresnel propagation towards various z propagation distances according to Eq. (9). Three different reconstruction planes are shown in Figure 2G, H and I. In each plane, a different letter is in focus as is indeed expected from a holographic reconstruction of an object with a volume.

4. FINCH for fluorescence objects

In Ref. [18] the FINCH system has been capable of recording multicolor digital holograms from objects emitting fluorescent light. The fluorescent light, specific to the emission wavelength of various fluorescent dyes after excitation of 3D objects, was recorded on a digital monochrome camera after reflection from the SLM. For each wavelength of fluorescent emission, the camera sequentially records three holograms reflected from the SLM, each with a different phase factor of the SLM's function. The three holograms are again superposed in the computer to create a complex-valued Fresnel hologram of each fluorescent emission without the twin image problem. The holograms for each fluorescent color are further combined in a computer to produce a multicolored fluorescence hologram and 3D color image.

An experiment showing the recording of a color fluorescence hologram was carried out [18] on the system shown in Figure 3. The phase constants of $\theta_{1,2,3}$=0°, 120°, 240° were introduced into the three quadratic phase functions. The other specifications of the system are: f_1=250 mm, f_2=150 mm, f_3=35 mm, d_1=135 mm, d_2=206 mm. The magnitude and phase of the final complex hologram, superposed from the first three holograms, are shown in Figure 4A and B, respectively. The reconstruction from the final hologram was calculated using the Fresnel propagation formula of Eq. (9). The results are shown at the plane of the front face of the front die (Figure 4C), and at the plane of the front face of the rear die (Figure 4D). Note that in each plane a different die face is in focus as is indeed expected from a holographic reconstruction of an object with a volume. The second set of three holograms was recorded via a red filter in the emission filter slider F_2 which passed 614 to 640 nm fluorescent light wavelengths with a peak wavelength of 626 nm and a bandwidth of 11 nm (FWHM). The magnitude and phase of the final complex hologram, superposed from the 'red' set, is shown in Figure 4E and F, respectively. The reconstruction results from this final hologram are shown in Figure 4G and H at the same planes as shown in Figure 4C and D, respectively. Finally, an additional set of three holograms was recorded with a green filter in emission filter slider F_2, which passed 500 to 532 nm fluorescent light wavelengths with a peak wavelength of 516 nm and a bandwidth of 16 nm (FWHM). The magnitude and phase of the final complex hologram, superposed from the 'green' set, is shown in Figure 4I and J, respectively. The reconstruction results from this final hologram are shown in Figure 4K and L at

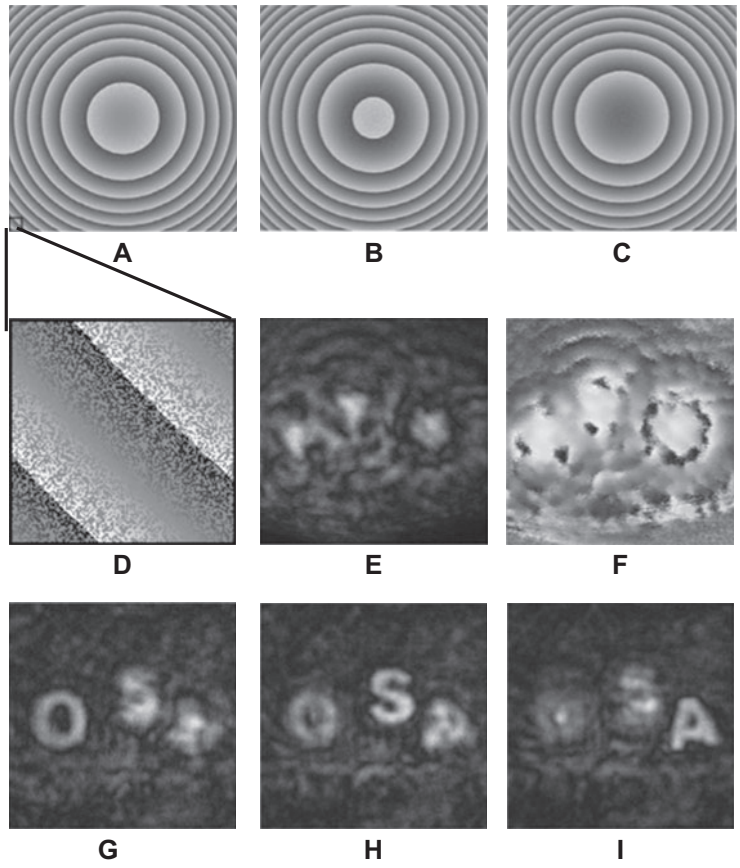

Figure 2 (A) Phase distribution of the reflection masks displayed on the SLM, with θ=0°, (B) θ=120°, (C) θ=240°. (D) Enlarged portion of (A) indicating that half (randomly chosen) of the SLM's pixels modulate light with a constant phase. (E) Magnitude and (F) phase of the final on-axis digital hologram. (G) Reconstruction of the hologram of the three letters at the best focus distance of 'O'. (H) Same reconstruction at the best focus distance of 'S' and (I) of 'A'.

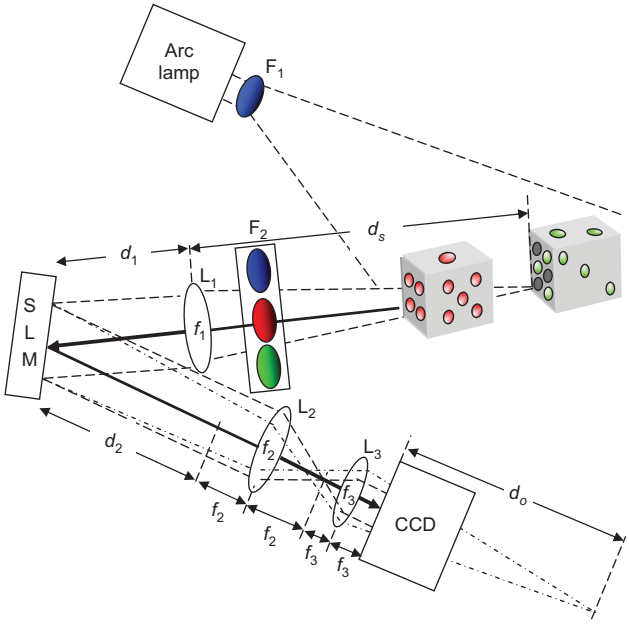

Figure 3 Schematics of the FINCH color recorder. SLM, spatial light modulator; CCD, charge-coupled device; L_1, L_2, L_3 are spherical lenses and F_1, F_2 are chromatic filters.

the same planes as shown in Figure 4C and D, respectively. Compositions of Figure 4C, G and K and Figure 4D, H and L are depicted in Figure 4M and N, respectively. Note that all colors in Figure 4 are pseudo-colors. These last results yield a complete color 3D holographic image of the object including the red and green fluorescence. Although the optical arrangement in this demonstration has not been optimized for maximum resolution, it is important to recognize that even with this simple optical arrangement, the resolution is good enough to image the fluorescent emissions with good fidelity and to obtain good reflected light images of the dice. Furthermore, in the reflected light images in Figure 4C and M, the system has been able to detect a specular reflection of the illumination from the edge of the front dice.

5. FINCHSCOPE: a holographic fluorescence microscope

The next system to be reviewed here is the first demonstration of a motionless microscopy system (FINCHSCOPE) based upon FINCH, and its use in recording high-resolution 3D fluorescent images of biological specimens [19]. By using high-numerical-aperture lenses, a spatial light modulator, a

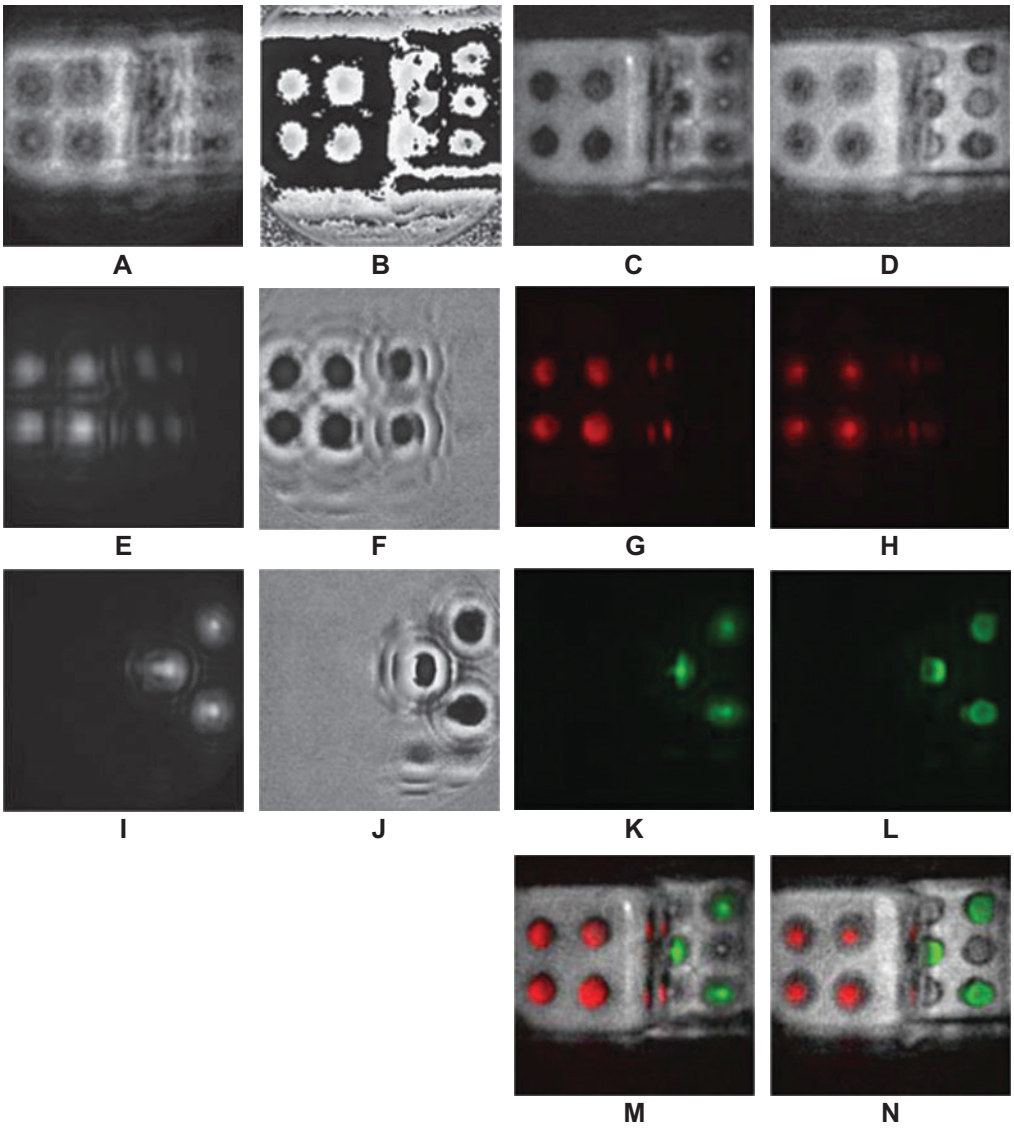

Figure 4 (A) Magnitude and (B) phase of the complex Fresnel hologram of the dice. Digital reconstruction of the non-fluorescence hologram: (C) at the face of the red dots on the die, and (D) at the face of the green dots on the die. (E) Magnitude and (F) phase of the complex Fresnel hologram of the red dots. Digital reconstruction of the red fluorescence hologram: (G) at the face of the red dots on the die and (H) at the face of the green dots on the die. (I) Magnitude and (J) phase of the complex Fresnel hologram of the green dots. Digital reconstruction of the green fluorescence hologram: (K) at the face of the red dots on the die, and (L) at the face of the green dots on the die. Compositions of (C), (G) and (K) and (D), (H) and (L) are depicted in (M) and (N), respectively.

charge-coupled device (CCD) camera and some simple filters, FINCHSCOPE enables the acquisition of 3D microscopic images without the need for scanning.

A schematic diagram of the FINCHSCOPE for an upright microscope equipped with an arc lamp source is shown in Figure 5. The beam of light that emerges from an infinity-corrected microscope objective transforms each point of the object being viewed into a plane wave, thus satisfying the first requirement of FINCH. An SLM and a digital camera replace the tube lens, reflective mirror and other transfer optics normally present in microscopes. Because no tube lens is required, infinity-corrected objectives from any manufacturer can be used. A filter wheel was used to select excitation wavelengths from a mercury arc lamp, and the dichroic mirror holder and the emission filter in the microscope were used to direct light to and from the specimen through infinity-corrected objectives.

The ability of the FINCHSCOPE to resolve multicolor fluorescent samples was evaluated by first imaging polychromatic fluorescent beads. A fluorescence bead slide with the beads separated on two separate planes was constructed. FocalCheck polychromatic beads (6 μm) were used to coat one side of a glass microscope slide and a glass coverslip. These two surfaces were juxtaposed and held together at a distance from one another of ~50 μm with optical cement. The beads were sequentially excited at 488, 555 and

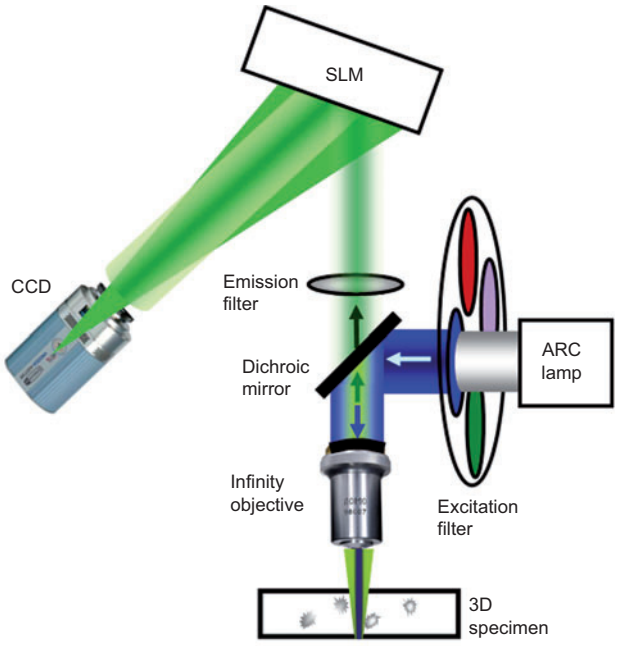

Figure 5 FINCHSCOPE schematic in upright fluorescence microscope. The upright microscope was modified with a reflective SLM positioned at a tilt angle of 11° to reflect emission light from the objective onto the camera.

640 nm center wavelengths (10–30 nm bandwidths) with emissions recorded at 515–535 nm, 585–615 nm and 660–720 nm, respectively. Figure 6A–D show reconstructed image planes from 6 µm beads excited at 640 nm and imaged on the FINCHSCOPE with a Zeiss PlanApo ×20, 0.75 Numerical Aperture (NA) objective. Figure 6A shows

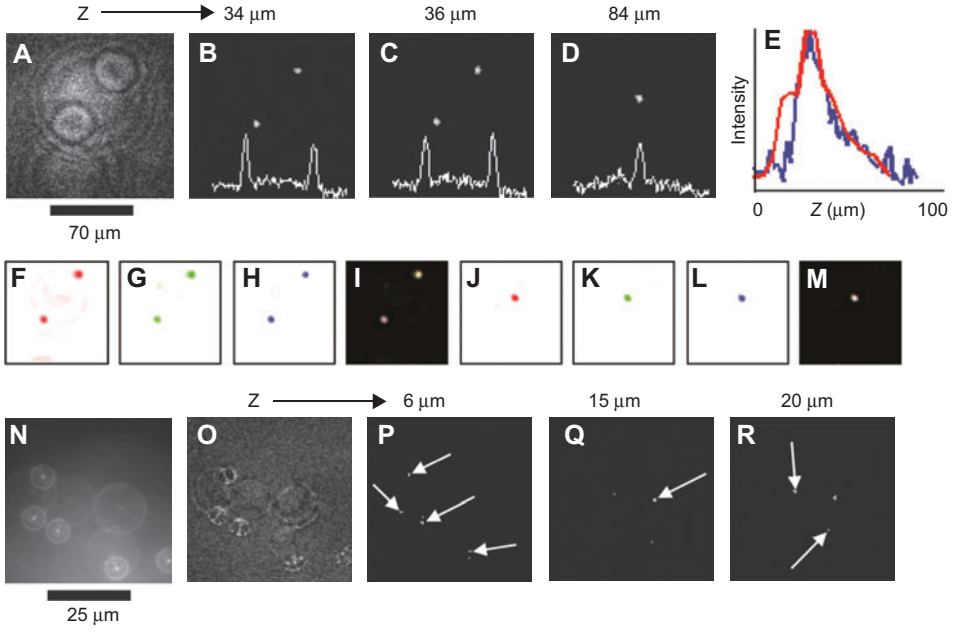

Figure 6 FINCHSCOPE holography of polychromatic beads. (A) Magnitude of the complex hologram 6 µm beads. Images reconstructed from the hologram at z distances of (B) 34 µm, (C) 36 µm and (D) 84 µm. Line intensity profiles between the beads are shown at the bottom of panels (B–D). (E) Line intensity profiles along the z axis for the lower bead from reconstructed sections of a single hologram (blue line) and from a widefield stack of the same bead (28 sections, red line). (F–H) Beads (6 µm) excited at 640, 555 and 488 nm with holograms reconstructed at planes B and (J–L) D. (I) and (M) are the combined RGB images for planes B and D, respectively. (N–R) Beads (0.5 µm) imaged with a 1.4-NA oil immersion objective: (N) holographic camera image; (O) magnitude of the complex hologram; (P–R) reconstructed image planes 6, 15 and 20 µm. Scale bars indicate image size.

the magnitude of the complex hologram, which contains all the information about the location and intensity of each bead at every plane in the field. The Fresnel reconstruction from this hologram was selected to yield 49 planes of the image, 2 μm apart. Two beads are shown in Figure 6B, with only the lower bead exactly in focus. The next image (Figure 6C) is 2 μm into the field in the Z-direction, and the upper bead is now in focus, with the lower bead slightly out of focus. The focal difference is confirmed by the line profile drawn between the beads, showing an inversion of intensity for these two beads between the planes. There is another bead between these two beads, but it does not appear in Figure 6B or C (or in the intensity profile), because it is 48 μm from the upper bead; it instead appears in Figure 6D (and in the line profile), which is 24 sections away from the section in Figure 6C. Note that the beads in Figure 6B and C are no longer visible in Figure 6D. In the complex hologram in Figure 6A, the small circles encode the close beads and the larger circles encode the distant central bead. Figure 6E shows that the Z-resolution of the lower bead in Figure 6B, reconstructed from sections created from a single hologram (blue line), is at least comparable to data from a widefield stack of 28 sections (obtained by moving the microscope objective in the Z-direction) of the same field (red line). The co-localization of the fluorescence emission was confirmed at all excitation wavelengths and at extreme Z limits as shown in Figure 6F–M for the 6 μm beads at the planes shown in Figures 6B, F–I, and 6D, J–M. In Figure 6N–R, 0.5 μm beads imaged with a Zeiss PlanApo ×63 1.4 NA oil immersion objective are shown. Figure 6N presents one of the holograms captured by the camera and Figure 6O shows the magnitude of the complex hologram. Figure 6P–R show different planes (6, 15 and 20 μm, respectively) in the bead specimen after reconstruction from the complex hologram of image slices in 0.5 μm steps. Arrows show the different beads visualized in different Z image planes.

6. Polarization method of multiplexing optical diffractive elements

FINCH creates holograms in a single beam system as a result of interference between spherical waves originating from every object point. In the above-mentioned configurations, we created a random constant phase mask so that with a phase-only SLM, the plane wave from an infinity corrected microscope objective could be directed to the camera along with the spherical wave created by the SLM. The use of a constant phase mask presents certain disadvantages in that it requires half the pixels on the SLM and also degrades the resolution of the mask which creates the spherical wave. Because only one linear polarization state on the liquid crystal based SLM can change the phase of incoming light, half of the randomly polarized fluorescent light striking the device can have quadratic phase modulation, whereas the other half is shifted by a constant phase, as shown in Figure 7A. However, the sensitivity of the SLM to a specific linear polarization also makes it possible to use the portion of the light not affected by the SLM to deliver the plane wave as shown in Figure 7B, and discussed below.

The following analysis summarizes Ref. [20] and refers to the system scheme shown in Figure 8, where it is assumed

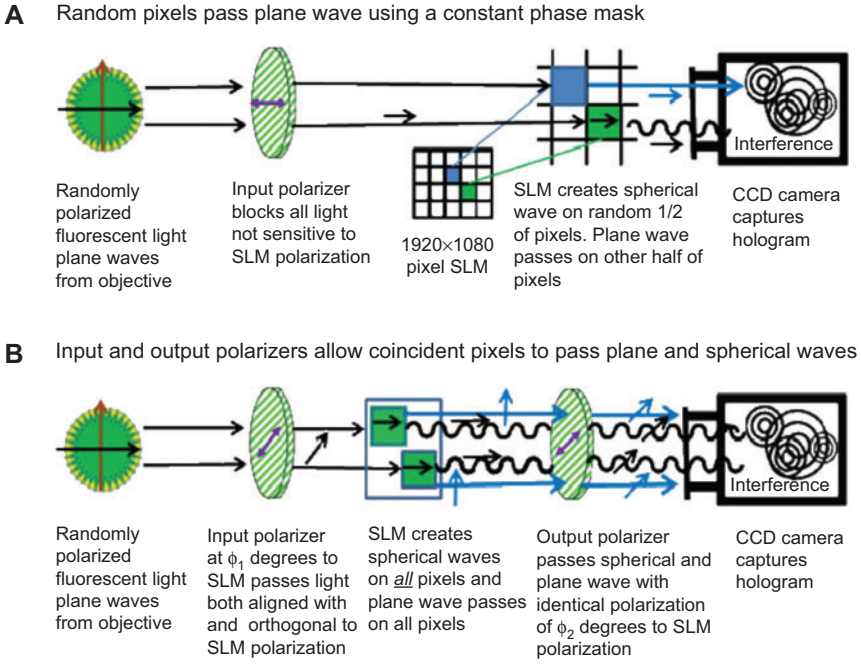

Figure 7 Comparison of using a constant phase mask (A) versus the polarization method (B) to select and separate the plane and spherical waves in FINCH holography. Note that when the polarization method is used, all the pixels on the SLM are used to create the diffractive lens pattern.

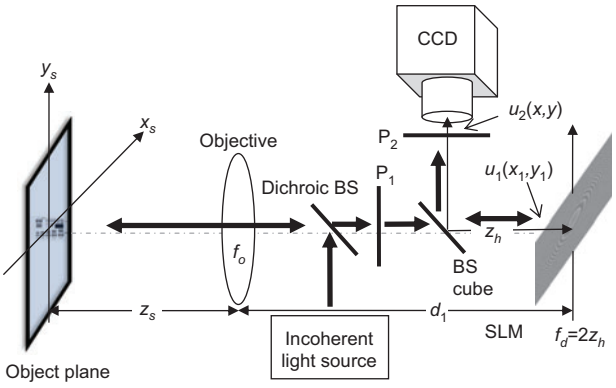

Figure 8 Microscope scheme. $P_{1,2}$ are the polarizers.

that the object is an infinitesimal point and therefore the result of this analysis is considered as a PSF. For an arbitrary object point at $(\bar{r}_s, -z_s)$ in a working distance z_s before the objective, where $\bar{r}_s=(x_s, y_s)$, the complex amplitude beyond the first polarizer, just before the SLM, is:

$$u_o(x_o,y_o)=C_1(\bar{r}_s)L\left(\frac{-\bar{r}_s}{z_s}\right)Q\left(\frac{1}{z_s}\right)Q\left(\frac{-1}{f_o}\right)*Q\left(\frac{1}{d_1}\right)(A_x\hat{x}+A_y\hat{y}) \quad (10)$$

where it is assumed that the polarizer axis is tilted in a ϕ_1 angle to the x axis, f_o is the focal length of the objective, d_1 is the distance between the objective and the SLM and A_x,A_y are the constant amplitudes in the x,y axes, respectively. $\hat{x}$ and $\hat{y}$ are unit vectors in the x,y directions, respectively. The SLM modulates the light in only a single linear polarization and in our case, without loss of generality, this axis is chosen to be x. The light polarized in y direction is reflected from the SLM with only a constant phase shift. Therefore, the complex amplitude on the output plane of the SLM is:

$$u_1(x_1,y_1)=C_1(\bar{r}_s)L\left(\frac{-\bar{r}_s}{z_s}\right)Q\left(\frac{1}{z_s}\right)Q\left(\frac{-1}{f_o}\right)*Q\left(\frac{1}{d_1}\right)\times\left[A_xB_Q\ \exp(i\theta)Q\left(\frac{-1}{f_d}\right)\hat{x}+A_yB_M\hat{y}\right] \quad (11)$$

where B_Q and B_M are complex constants. The complex amplitude after passing the second polarizer, with axis angle of ϕ_2 to the x axis, has linear polarization in the direction of the polarizer axis. Therefore, we can abandon the vector notation and express the complex amplitude beyond the second polarizer, on the CCD plane, as:

$$u_2(x_2,y_2)=C_1(\bar{r}_s)L\left(\frac{-\bar{r}_s}{z_s}\right)Q\left(\frac{1}{z_s}\right)Q\left(\frac{-1}{f_o}\right)*Q\left(\frac{1}{d_1}\right)\times\left[A_yB_M\sin\phi_2+A_xB_Q\ \exp(i\theta)Q\left(\frac{-1}{f_d}\right)\cos\phi_2\right]*Q\left(\frac{1}{z_h}\right) \quad (12)$$

where z_h is the distance between the SLM and the CCD. The intensity of the recorded hologram is:

$$I_P(x_2,y_2)=\left|C_1(\bar{r}_s)L\left(\frac{-\bar{r}_s}{z_s}\right)Q\left(\frac{1}{z_s}\right)Q\left(\frac{-1}{f_o}\right)*Q\left(\frac{1}{d_1}\right)\times\left[A_yB_M\sin\phi_2+A_xB_Q\ \exp(i\theta)Q\left(\frac{-1}{f_d}\right)\cos\phi_2\right]*Q\left(\frac{1}{z_h}\right)\right|^2 \quad (13)$$

Following the calculation of Eq. (13), the intensity on the CCD plane, the reconstruction distance of the object point and the transverse location $\bar{r}_r=(x_r, y_r)$, are given by Eqs. (4), (5) and (6), respectively. The polarization angles ϕ_1 and ϕ_2 are chosen to maximize the interference terms [the second and third terms in Eq. (4)]. Their precise values depend on the values of the constants $|B_Q|$ and $|B_M|$. In Ref. [20] we have chosen their values empirically by picking the angles that yield the best reconstructed image.

The optimal conditions for imaging the fluorescent USAF slide with both the constant phase mask method and the polarization method were compared. The results demonstrate the superiority of the polarization method. Figure 9 shows the optimal plane of focus from image reconstructions made from holograms captured with both methods. The conditions were identical, using an 800-mm focal length diffractive lens pattern and with the camera positioned 400 mm from the SLM. In Figure 9A, the holograms were captured with a 37% constant phase mask and with the input and output polarizers set at 0° (i.e., parallel with the SLM polarization). In Figure 9B, the holograms were captured using the polarization method, without any constant phase mask and with the polarizers set at 60° to the x axis.

Imaging pollen grains has been a convenient way to compare the performance of microscopes on biological samples. We compared the performance of the new dual-polarizers method to our previous constant phase mask method. As with the USAF slide, the results with the polarizers method were much better for the exact same field as shown in Figure 10. Also note the improved resolution of the two pollen grains along the edges of the field with the polarization method. The slight ghost images that can be seen in Figure 10 are not inherent to FINCH, because ghost images have been viewed even when the SLM has been used as a flat mirror or even when it has been replaced by a regular flat mirror and a refractive lens (data not shown). We suspect that these ghost images appear

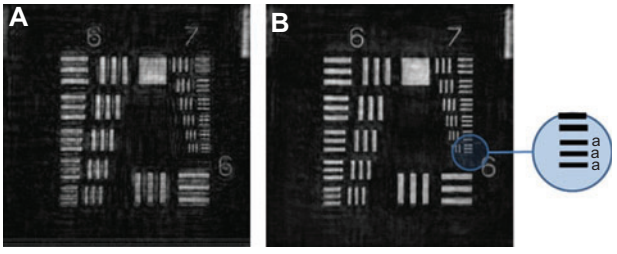

Figure 9 Best plane of focus reconstruction from holograms of the fluorescent USAF test slide using the constant phase mask technique and the polarizers method. (A) Static mask. (B) Input and output polarizers at 60°. Bars labeled 'a' are 1.6 μm thick and there is 2.5 μm distance between each of the three bars.

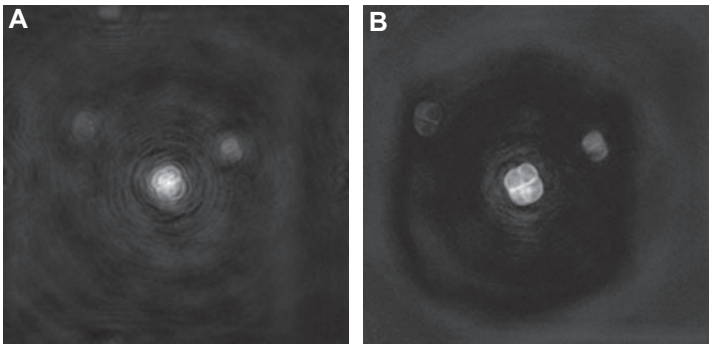

Figure 10 Best plane of focus from holograms of a pollen grain test slide using the constant phase mask technique and the dual polarizers method. (A) Constant phase mask. (B) Polarizers at 60°.

because of light reflections from the beam splitter. There were no ghost images in images taken with a 45° flat mirror and refractive lens, but that configuration was not suitable for this FINCH.

7. Resolution beyond the Rayleigh limit by FINCH

In this section, we present theoretical and experimental data from Ref. [21] that show that FINCH imaging can exceed standard optical imaging system resolution. Particularly, we address the question of which of the systems, FINCH or a conventional glass lens-based imaging system, can resolve better. There is not an obvious answer to this question because FINCH has unique properties that do not exist in conventional optical imaging systems; on the one hand, the FINCH hologram is recorded by incoherent illumination, but on the other hand this hologram is reconstructed by the Fresnel back-propagation process, exactly as is done with a typical coherent Fresnel hologram. So the question is whether FINCH behaves like a coherent or incoherent system, or whether it has its own unique behavior. Knowing that the difference between coherent and incoherent imaging systems is expressed, among others, by their different modulation transfer function (MTF), the more specific question is what type of MTF characterizes FINCH. Does FINCH have an MTF of a coherent or incoherent imaging system, or does it have its own typical MTF? The answer to this last question can determine the answer to the resolution question. In this section, we analyze the transverse resolution of FINCH and show here, both theoretically and experimentally, that FINCH imaging significantly exceeds the resolution of a conventional microscope optical imaging system.

FINCH, in the present model, creates holograms in a single-channel system as a result of interference between two waves originating from every object point located in front of a collimating lens. The following analysis refers to the system scheme shown in Figure 11A, where, as before, it is assumed that the object is an infinitesimal point and therefore the result of this analysis is considered as a PSF. For simplicity, we assume that the object point is located at $\overline{r}_s=(x_s, y_s)$ on the front focal plane of the collimating lens L_1 (an objective lens in the case of an infinity corrected microscope system). For an infinitesimal object point with the complex amplitude $\sqrt{I_s}$, the intensity of the recorded hologram is:

$$I_H(u,v)=\left|\sqrt{I_s}C(\overline{r}_s)L\left(\frac{-\overline{r}_s}{f_o}\right)Q\left(\frac{1}{f_o}\right)Q\left(\frac{-1}{f_o}\right)*Q\left(\frac{1}{d}\right)\right.$$
$$\left.\left[B+B'exp(i\theta)Q\left(\frac{-1}{f_d}\right)\right]*Q\left(\frac{1}{z_h}\right)P(R_H)\right|^2, \qquad (14)$$

where f_o is the focal length of lens L_1, d is the distance between the lens L_1 and the SLM, z_h is the distance between the SLM and the camera, $\overline{\rho}=(u, v)$ are the coordinates of the camera plane and B, B' are constants. The function $P(R_H)$ stands for the limiting aperture of the system, where it is assumed that the aperture is a clear disk of radius R_H determined by the overlap area of the two interfering beams on the camera plane. The expression in the square brackets of Eq. (14) describes the transparency of the SLM. This transparency is a combination of a constant valued mask with a diffractive positive spherical lens of focal length f_d. In the previous sections, we presented two methods to display these two masks on the same SLM. The older, and less efficient, method is to randomly allocate half of the SLM pixels to each of the two masks [17–19].

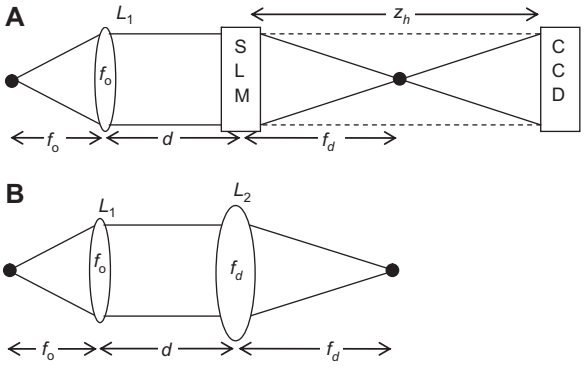

Figure 11 Comparisons of the optical configuration for (A) FINCH with only one diffractive lens and (B) a regular optical imaging system with the same parameters used in (A).

Lately [20], and as described in section 6, we have learned that a better way is by use of a positive lens mask over the whole SLM and light with two mutually orthogonal polarization components, one of which is parallel to the polarization of the SLM and the other which is orthogonal to it, so that the interference happens between the projections of each polarization component of the light beam on the crossing angle between the two orthogonal polarizations.

On the camera detector, only the area of the beam overlap, denoted by the area of $P(R_H)$, is considered as part of the hologram. Three holograms of the form of Eq. (14) with three different values of the angle θ are recorded and superposed to obtain a complex hologram of the object point, given by:

$$H(\overline{\rho})=C' I_s P(R_H) L\left(\frac{\overline{r}_r}{z_r}\right) Q\left(\frac{1}{z_r}\right), \tag{15}$$

where C' is a constant and z_r is the reconstruction distance from the hologram plane to the image plane calculated to be:

$$z_r=\pm|z_h-f_d|. \tag{16}$$

$\overline{r}_r$ is the transverse location of the reconstructed image point calculated to be:

$$\overline{r}_r=(x_r, y_r)=\overline{r}_s\frac{z_h}{f_o}. \tag{17}$$

From Eq. (17) it is clear that the transverse magnification is $M_T=z_h/f_o$. The PSF of the complete system is obtained by reconstructing digitally the Fresnel hologram given in Eq. (15) at a distance z_r from the hologram plane. The expression of the hologram in Eq. (15) contains a transparency of a positive lens with focal distance z_r and hence, according to Fourier optics theory [23], the reconstructed image is:

$$\begin{aligned} h_F(\overline{r}) &= C' I_s \nu\left[\frac{1}{\lambda z_r}\right]\mathcal{F}\left\{L\left(\frac{\overline{r}_r}{z_r}\right)P(R_H)\right\} \\ &= C'' I_s Jinc\left(\frac{2\pi R_H}{\lambda z_r}\sqrt{(x-M_T x_s)^2+(y-M_T y_s)^2}\right), \end{aligned} \tag{18}$$

where C'' is a constant, $\mathcal{F}$ denotes Fourier transform, ν is the scaling operator such that $\nu[a]f(x)=f(ax)$, $\overline{r}=(x, y)$ are the coordinates of the reconstruction plane, *Jinc* is defined as $Jinc(r)=J_1(r)/r$ and $J_1(r)$ is the Bessel function of the first kind, of order one.

Eq. (18) describes the 2D PSF of the complete FINCH from recording to reconstructing stages. Recalling that the object is a collection of infinitesimal incoherent light points which cannot interfere with each other, we realize that each independent object point is imaged to an image of the form of Eq. (18). The complete image of many object points is a convolution integral between the object denoted by intensity distribution $I_s(\overline{r})$ with the PSF shown in Eq. (18), as follows:

$$I_i^L(\overline{r})=I_s(\overline{r})*h_F(\overline{r}). \tag{19}$$

Eq. (19) indicates that FINCH is a linear invariant system for the quantity of light intensity. However, because h_F is in general a complex valued function, I_i^L might also be a complex valued function. This observation does not contradict any physical law because the reconstruction is done digitally by the numerical algorithm of the Fresnel back-propagation [23]. The superscript L is added to the intensity obtained by Eq. (19) to distinguish it from the non-linear reconstruction discussed next.

In case the hologram is reconstructed optically by illuminating the hologram with a coherent plane wave, the output intensity is:

$$I_i^N(\overline{r})=\left|I_s(\overline{r})*h_F(\overline{r})\right|^2. \tag{20}$$

I_i^N denotes intensity of the optical reconstruction, or non-linear digital reconstruction as is demonstrated in the experimental part of this study. This image is not linear in relation to the gray levels of $I_s(\overline{r})$, but in some cases, for instance, binary objects whose images are not distorted by the non-linear operation, I_i^N is preferred over I_i^L because the side lobes of h_F are suppressed by the square operation, which results in improved image contrast.

The width of the PSF in every imaging system determines the resolution of the system. The width of the PSF is chosen herein as the diameter of the circle created by the first zero of the *Jinc* function of Eq. (18). This diameter remains the same for both the linear and non-linear reconstructions, and is equal to $1.22\lambda z_r/R_H$. According to Eq. (16), $z_r=|z_h-f_d|$ and therefore, based on a simple geometrical consideration, the radius of the hologram, which is the radius of the overlap area between the plane and the spherical beams, is:

$$R_H=\begin{cases} R_o\dfrac{|z_h-f_d|}{f_d} & f_d\geq\dfrac{z_h}{2} \\ R_o & Otherwise, \end{cases} \tag{21}$$

where R_o is the radius of the smallest aperture in the system up to, and including, the SLM. For $f_d<z_h/2$ the projection of the spherical wave exceeds beyond the plane wave projection and therefore the radius of the overlap remains as R_o. Consequently, the width of the PSF for the regime of $f_d\geq z_h/2$ is:

$$\Delta=\frac{1.22\lambda z_r}{R_H}=\frac{1.22\lambda|z_h-f_d|f_d}{R_o|z_h-f_d|}=\frac{1.22\lambda f_d}{R_o}. \tag{22}$$

This PSF has exactly the size one would expect to see in the output of a regular imaging system shown in Figure 11B. At first glance, one might conclude that because the two systems have the same PSF, with the same width, their resolving power is the same. However, Eq. (17) indicates that the location of the image point in the output plane of FINCH is at $\overline{r}_s\, z_h/f_o$. This is, in general, different than the location of the image point of the imaging system of Figure 11B, which is $\overline{r}_s\, f_d/f_o$. In other words, if the two systems observe the same two object points, the size of all the image points in the two systems is the same, but the gap between the two image points differs between the two compared systems. The two point gap of FINCH and of the regular imaging system differ by the ratio of z_h/f_d. Recalling that resolution is related to the gap between image points, as is manifested by the well-known

Rayleigh criterion, we realize that if $z_h/f_d>1$, then FINCH can resolve better than a regular system. This is because in FINCH, the gap between every two image points is larger by a factor of z_h/f_d compared to the two point gap of a regular imaging system with the same numerical aperture. Moreover, increasing the ratio z_h/f_d in FINCH increases the resolution, where the maximum resolving power is achieved for the ratio $z_h/f_d=2$. Beyond this limit the radius of the hologram is not increased further and keeps the maximum radius of R_o. That is again because the size of the spherical wave projection on the detector exceeds the plane wave projection, so the overlap area remains within the same circle with the radius of R_o.

To further investigate the properties of FINCH in comparison to a regular imaging system, one needs to equalize the size of both overall output images. Recall that the FINCH's overall image of many points is bigger by the factor $z_h/f_d>1$, hence the output image with FINCH should be shrunk by this factor. Thus, when the FINCH image is shrunk by the factor of z_h/f_d the overall image of both systems is the same and therefore can be compared on an equal basis. However, the result of shrinking the entire image causes the PSF size of FINCH to be narrower by the factor of z_h/f_d in comparison to that of a regular imaging system. Therefore, the effective width of the PSF of FINCH is:

$$\Delta_e=\begin{cases}\dfrac{1.22\lambda z_r f_d}{R_H z_h}=\dfrac{1.22\lambda f_d^2}{R_o z_h} & f_d\geq\dfrac{1}{2}z_h \\ \dfrac{1.22\lambda z_r f_d}{R_o z_h}=\dfrac{1.22\lambda f_d\left(1-f_d/z_h\right)}{R_o} & 0<f_d<\dfrac{1}{2}z_h.\end{cases} \tag{23}$$

According to Eq. (23), the PSF width and consequently the resolution are dependent on the ratio z_h/f_d for all values of f_d. The minimum width of the PSF is obtained for $z_h/f_d=2$, and this width is $\Delta_e=0.61\cdot\lambda f_d/R_o$ (or $0.61\cdot\lambda f_o/R_o$ in the object domain), which is half the width of the PSF of a regular imaging system (shown in Figure 11B) with the same numerical aperture. The effective PSF of FINCH for the ratio $z_h/f_d=2$ is now:

$$h_F\left(\overline{r}\right)=C''I_s Jinc\left(\frac{4\pi R_o}{\lambda f_d}\sqrt{\left(x-M_T x_s/2\right)^2+\left(y-M_T y_s/2\right)^2}\right). \tag{24}$$

In terms of resolution, the improvement of FINCH in comparison to a regular incoherent microscope is more than a factor of 1 but somewhat less than a factor of 2 because the PSF of FINCH shown in Eq. (24) has the shape of that of a coherent system. To estimate the resolution improvement we recall that according to the Rayleigh criterion, two points are resolved if the dip between their images is more than approximately 27% of the maximum intensity [23]. A simple numerical calculation indicates that in order to create a dip of not less that 27% between two functions of the form of Eq. (24), the minimal distance between them should be no less than $0.61\cdot\lambda f_d/(1.4\cdot R_o)$ and $0.61\cdot\lambda f_d/(1.5\cdot R_o)$ in cases of linear and non-linear reconstruction, respectively. Therefore, the resolution improvement of FINCH over a regular incoherent microscope is approximately a factor of 1.4 and 1.5 for linear and non-linear reconstruction, respectively. The FINCH's resolution improvement over a coherent imaging system is a factor of 2.

According to Eq. (18), the PSF of FINCH is obtained as the scaled Fourier transform of the system aperture, exactly as is the case of a coherent imaging system. Therefore, the shape of the MTF of FINCH is similar to the shape of the system aperture, i.e., a uniform clear disc shape. However, the cut-off frequency of FINCH is different by the ratio of z_h/f_d than that of a regular coherent imaging system, and can be twice as high in the optimal setup of $z_h/f_d=2$. Moreover, FINCH with the ratio $z_h/f_d=2$ has the same cut-off frequency as an incoherent imaging system, but unlike the later system, the MTF of FINCH is uniform over all the frequencies up to the cut-off frequency.

We conclude that FINCH is superior in terms of resolution over both coherent and incoherent imaging systems. In fact, FINCH enjoys the best of both worlds; it has a cut-off frequency of an incoherent system with the same numerical aperture, and a uniform MTF like a coherent system. Figure 12 summarizes the main properties of FINCH in comparison to either coherent or incoherent imaging systems. Looking at Figure 12, one can conclude that, in addition to the two well-known types of imaging systems, coherent and incoherent, there is a third type which can be denoted as a hybrid imaging system characterized by FINCH, because it associates incoherent recording with coherent reconstruction. The hybrid imaging system is linear in the intensity but its PSF is in general a complex valued function. Its MTF has the shape of the system aperture with a cut-off frequency that can be twice as large as that of a coherent imaging system with the same numerical aperture. In comparison to an incoherent system we see that both systems have the same bandwidth but FINCH does not attenuate the intensity of spatial frequencies greater than zero, as the incoherent imaging system does.

The superiority of FINCH in the resolution aspect is explained by the fact that the hologram of each object point is an interference result between two beams, both originated from this same point. The information about the point location is stored in the phase of both beams. During the wave interference, under the condition $z_h/f_d>1$, the two phases have the same sign and therefore they are summed such that the resulting linear phase function has a higher slope than in case of recording a coherent hologram with a non-informative reference beam. Therefore, as a result of the phase gaining, the image point location is farther from some arbitrary reference point than in the case of a regular imaging system, and therefore the image magnification is higher in FINCH. As a result, the separation between points is larger in FINCH and this feature is translated to better overall resolution. In the regime of $z_h/f_d<1$ the two summed phases have an opposite sign such that the resulting overall phase is demagnified, the gap between various image points, and consequently the resolution, are smaller in comparison to a conventional imaging system with the same numerical aperture.

Based on the discussion above, it is clear that the optimal ratio with regard to resolution between z_h and f_d is $z_h/f_d=2$. However, this optimal ratio is obtained in the specific setup shown in Figure 11A and the question is whether there is a more general configuration of FINCH in which the same

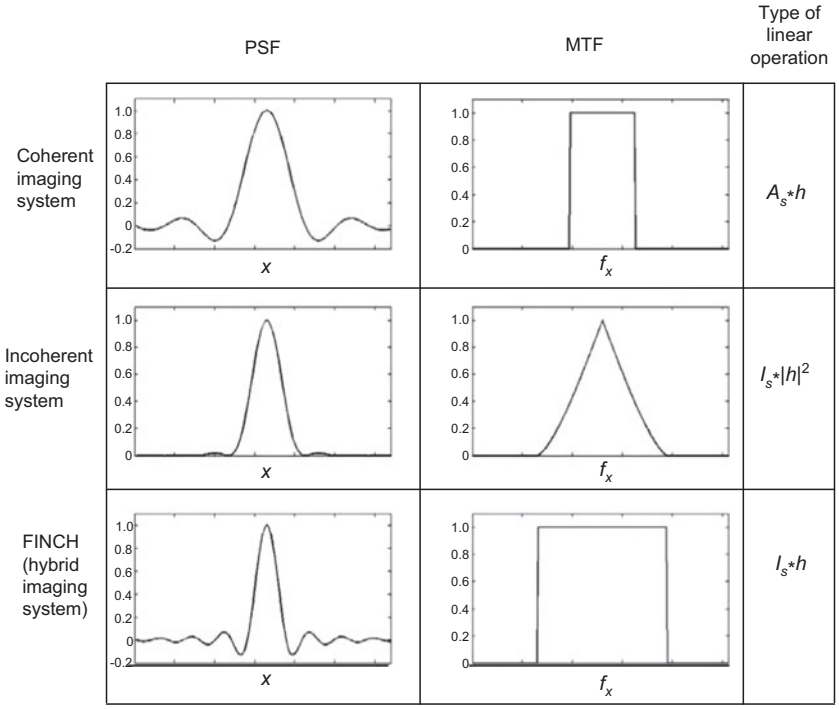

Figure 12 Summary of the main features of the three linear systems discussed in the text. A_s and I_s denote a complex amplitude and intensity of the input object, respectively. x and f_x are the space and the spatial frequency coordinate, respectively.

resolution can be achieved. In the following subsection, we try to answer this question.

According to Eq. (23) the effective resolution of FINCH is:

$$\Delta_e = \frac{1.22\lambda z_r f_d}{R_H z_h} . \tag{25}$$

To improve resolution one should look for a configuration with higher R_H and z_h/f_d and with a z_r that grows less than the other two factors. Such configuration might be the one shown in Figure 13A, in which the FINCH is generalized in the sense that the constant phase on the SLM is replaced with a negative lens with f_2 focal distance. When the various parameters are chosen such that there is a perfect overlap between the two spherical waves on the camera plane, R_H and the ratio z_h/f_d indeed become higher. The new z_r is calculated from a similar equation to Eq. (14), in which in addition to the constant B there is a transfer function of a negative lens as the following:

$$I_H(u,v) = \left| \sqrt{I_s} C(\bar{r}_s) L\left(\frac{-\bar{r}_s}{f_o}\right) Q\left(\frac{1}{f_o}\right) Q\left(\frac{-1}{f_o}\right) * Q\left(\frac{1}{d}\right) \times \left[BQ\left(\frac{1}{f_2}\right) + B' exp(i\theta)\, Q\left(\frac{-1}{f_d}\right) \right] * Q\left(\frac{1}{z_h}\right) P(R_H) \right|^2 . \tag{26}$$

z_r calculated from Eq. (26) is:

$$z_r = \pm \left| \frac{(z_h - f_d)(z_h + f_2)}{f_d + f_2} \right| . \tag{27}$$

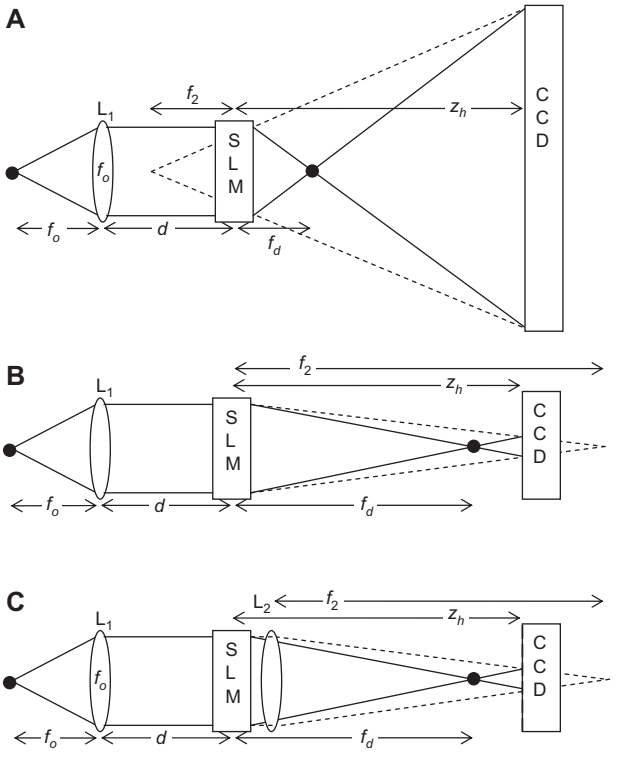

Figure 13 (A) FINCH with two diffractive lenses, one is positive and the other is negative. (B) FINCH with two diffractive lenses, both are positive. (C) A practical setup that emulates the setup of (B), with one positive diffractive lens displayed on the SLM and one positive glass lens placed near to the SLM.

The transverse magnification remains $M_T=z_h/f_o$ as before. Next, we make use of the fact that the two spherical waves perfectly overlap on the camera plane, and based on simple geometrical considerations, the following two relations are obtained:

$$R_H=R_o\frac{z_h-f_d}{f_d}, \tag{28}$$

$$\frac{z_h-f_d}{f_d}=\frac{z_h+f_2}{f_2}. \tag{29}$$

Substituting Eqs. (27)–(29) into Eq. (25) yields that effective width of FINCH's PSF in the general configuration is:

$$\Delta_e=\frac{0.61\cdot\lambda f_d}{R_o}. \tag{30}$$

This is the same result obtained with the configuration of Figure 11A for $z_h/f_d=2$. The conclusions are as follows: (i) FINCH resolution in any configuration is limited by the value of Δ_e given in Eq. (30). This conclusion is expected because any configuration of FINCH does not enable any new information, or more spatial frequencies, to enter into the system, and therefore there is no reason for any further resolution improvement beyond the superior result given in Eq. (30). (ii) The optimal configuration can be obtained in many forms as long as the overlap between the two different beams on the camera plane is perfect. This conclusion is true even if both diffractive lenses on the SLM are positive, where one is focused before the camera and the other beyond it, as is shown in Figure 13B. In that case the z_r is calculated by the same method to be:

$$z_r=\pm\left|\frac{(z_h-f_d)(z_h-f_2)}{f_d-f_2}\right|, \tag{31}$$

and the radius of the hologram under the perfect overlap condition is the same as is given in Eq. (28), where the following relation also exists:

$$\frac{f_2-z_h}{f_2}=\frac{z_h-f_d}{f_d}. \tag{32}$$

Substituting Eqs. (28), (31) and (32) into Eq. (25) again yields the same effective resolution as is given in Eq. (30). Here again the optimal resolution can be achieved. The possible advantages of the configurations of Figures 11A, 13A and B were investigated in Ref. [22]. Note that displaying two different diffractive lenses on randomly distributed pixels of the same SLM could result in reduced efficiency from both lenses, because only half of the SLM pixels are available for each lens [17–19]. Therefore, a glass spherical lens should be added to the system which together with the SLM (on which the pattern of a sum of constant and quadratic phase functions are displayed) creates an equivalent system of Figure 13B. This system is depicted in Figure 13C. The purpose of the additional glass lens is to convert the plane wave, reflected from the SLM, into a converging spherical wave which interferes with the other spherical wave to create the hologram.

The purpose of the following experiments was to test the theoretical predictions. Specifically, we wanted to determine the relationship between z_h/f_d and FINCH resolution and to compare the resolution of FINCH microscopy at optimal z_h/f_d to that of optical microscopy. The infinity beam of the sample imaged with a microscope objective is directed to an SLM and is split into two beams which interfere at a camera to create a hologram. The microscope configuration schematically shown in Figure 14 used for these experiments was built upon our laboratory's previous concepts and designs for implementing FINCH in a microscope [19, 20] with some important additions and modifications. In the experiments described here, the identical smallest features on the highest resolution USAF chart were imaged at the plane of focus by three methods and compared: (i) conventional high resolution fluorescence microscopy with all glass optics including a matched and properly configured microscope tube lens, (ii) microscopy which utilized the SLM as a tube lens to focus the image upon the camera, and (iii) holograms captured with FINCH and reconstructed at the best plane of focus.

To simplify analysis and be able to compare image resolution between conventional fluorescence microscopy (which only resolves a single focal plane) and FINCH, a USAF negative test slide with a single plane of focus that contained group 9 features as small as 645 lp/mm (0.78 μm feature size) was used. The slide was placed upon a fluorescent plastic slide, as previously described [20], so that the negative features were fluorescent. A No. 1 coverslip was placed on the slide with microscope immersion oil between the coverslip and the test slide. There was an air interface between the objective and the top of the coverslip. The USAF pattern was adjusted to the plane of focus of the objective and kept in that position for all of the imaging experiments.

An important difference in the configuration from previous designs is that the SLM was positioned at a 45° angle and the system was designed for ready switching between ocular or camera viewing of the sample fluorescence and holography without disturbing the position or focus of the sample. This new microscope configuration was constructed on the stand of an upright Zeiss Axiophot fluorescence microscope. The binocular head with camera port and tube lens of the microscope was removed and the components needed for FINCH holography and viewing of the sample were attached to the microscope in its place. The remaining components of the microscope were not altered. An AttoArc 100 watt mercury arc lamp was used as the excitation source and the excitation was controlled by an electronic shutter. In these experiments, an air 20X, 0.75 NA objective was used. The emission filter was a 570-nm center, 10-nm bandpass filter for the FINCH images and the images taken with the SLM as a tube lens. In experiments not shown, as expected, the resolving power of the objective-tube lens combination was confirmed to be the same with the emission filter as with the 10-nm bandpass filter. This is because the Nikon Plan Apo objective-tube lens combination is achromatic. Careful alignment of the SLM in all directions was essential to prevent any image degradation. Furthermore, the SLM firmware was modified to give a 2π phase shift over its range at a 45° angle and the Fresnel patterns displayed on the SLM were

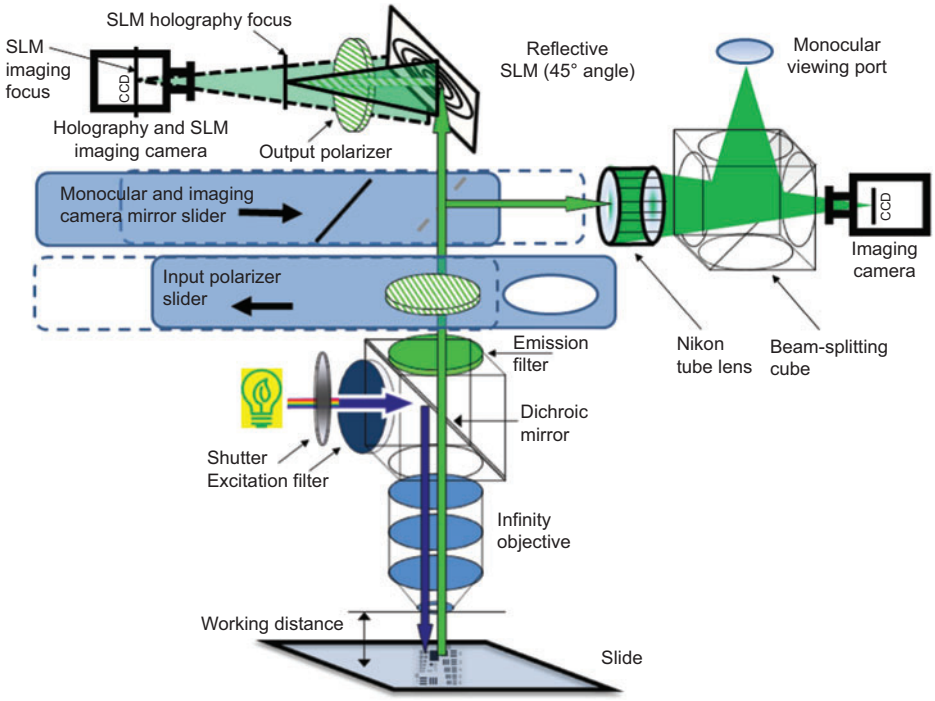

Figure 14 Schematic representation of the microscope for comparison of FINCH to standard fluorescence microscopy on the same identical sample without change in position or focus. The position of the two sliders and the diffractive lens pattern displayed on the SLM determines the imaging mode selected. The position of the sliders is shown for FINCH. Imaging of the sample using the SLM as a tube lens was possible by moving the input polarizer to the open position and displaying a diffractive lens pattern with a focal length equivalent to the distance between the SLM and camera. Reversing the position of the two sliders shown in the schematic allowed direction of the fluorescent emission to pass through the tube lens to the monocular viewing port and associated imaging camera for conventional fluorescence microscopy.

adjusted for the 45° angle. Input and output polarizers were rotated 45° along the optical axis as previously described in section 6 for improved resolution, so that all the pixels on the SLM were utilized to create the two interfering wavefronts. A calibrated iris was attached to the back aperture of the objective so that the back aperture could be varied from 3 mm to 12 mm to reduce the resolution of the objective so that FINCH imaging could be directly compared to optical microscopy at different effective objective NAs. Removal of the iris enabled imaging with the full 16 mm back aperture of the objective. To compare imaging performance between regular microscopy with that of FINCH, the microscope was configured so that a precision mirror on a roller-ball bearing slider could be inserted into the emission beam path without disturbing the location or focus of the sample or the setting of the back aperture of the objective. Once the mirror was in place, the emission light was simultaneously directed through a tube lens and beam splitting cube to another of the same model camera that was used for holography. Furthermore, an ocular positioned on the beam splitting cube allowed direct viewing of the sample under observation. An in focus image on the camera used for holography was obtained when the focal length of the diffractive lens pattern displayed on the SLM was equivalent to the distance between the SLM and camera.

The ability of the camera to resolve the fine fringes of the hologram has a significant effect on the ability of FINCH to resolve small objects. Because of this, we moved the camera away from the SLM until we reached a z_h position of 1380 mm at which we were able to resolve the smallest features in the USAF pattern using FINCH with z_h/f_d=2. The size of the acquired hologram is equal to the size of the diffractive Fresnel lens displayed on the SLM. As shown in the left panel of Figure 15, the microscope image of the small features in groups 8 and 9 (shown in the red box), under standard imaging conditions with a tube lens and with a 5-mm aperture over the back of the objective lens, was rather small and needed to be zoomed in to see them as shown in the middle image of Figure 15, whereas the FINCH images needed to be zoomed and cropped much less due to the magnification imposed by the long SLM-CCD distance. As can be seen, the small features were not well resolved by regular microscopy; however, imaging with FINCH clearly resolved the small features as shown in the right panel of Figure 15.

The USAF resolution target used in these experiments contains the smallest features available. To compare FINCH resolution in a very controlled manner to standard microscopic imaging, we imaged this target with the Nikon 20X 0.75 NA objective which had a 16-mm back aperture. We then installed a calibrated iris on the back aperture of the objective and systematically reduced the aperture from 12 mm to 3 mm. At each reduction in the back aperture, we took standard microscope images, images using the SLM as the tube lens and FINCH holographic images which were reconstructed as either linear or non-linear images as described above.

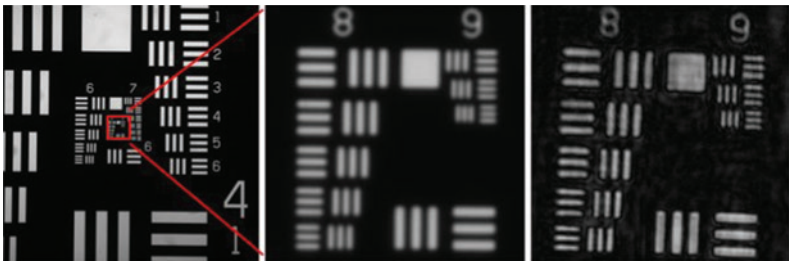

Figure 15 Representative full field USAF slide images captured in standard microscope operating mode (left panel). (Middle panel) Zoomed-in group 8 and 9 features from full field standard microscope image. (Right panel) Digitally linear reconstructed FINCH image of the small central pattern shown in the middle image, slightly cropped to match the middle image. All images were taken with a 5-mm aperture placed at the back plane of the objective.

An analysis of this experiment is shown in Figure 16. The plot of Figure 16 shows the visibility in the smallest group of lines versus the diameter of the back aperture, where the visibility defined as $(I_{max}-I_{min})/(I_{max}+I_{min})$ is a standard quantity used to characterize resolution. In this work [21], we examined visibility of the horizontal features in group 9, element 3, i.e., the smallest features. To define I_{max}, we located the row of pixels in each of the three features that had the highest summed intensity. We then averaged all the pixel values from those rows. To define I_{min}, we located the row of pixels in each of the gaps between the features that had the lowest summed intensity, and then averaged the pixel values from those rows. Visual inspection of the images and the visibility calculations demonstrate that FINCH images resolve the smallest features better than images from the comparable standard microscope configuration at all effective NAs of the objective. Using the SLM as a tube lens produced images which had similar resolution to the glass tube lens up to an aperture of 8 mm, the approximate minimum size of the aperture of the SLM when viewed at a 45° angle in our setup.

We then investigated the relationship between resolution and z_h/f_d, which we call z-ratio, using a reduced aperture of 5 mm because this dramatically reduced the imaging resolution of the objective under normal microscope conditions. Images at varying z-ratios from 0.85 to 2.4 were recorded. Visual inspection of the images shows that the resolution continues to improve as the z-ratio increases from 0.85 and reaches a peak around z-ratio=1.8±0.2. Visibility data is presented in Figure 17. The maximum is not exactly at $z_h/f_d=2$ because as already indicated in Ref. [20], the SLM has inherent spherical-like curvature which introduces an effective positive spherical lens of approximately 8 m focal length. In other words, instead of a system of the type shown in Figure 11A in which the maximum resolution is obtained at $z_h/f_d=2$, effectively there is a system of the type shown in Figure 13C in which there is an additional lens in the system (the inherent

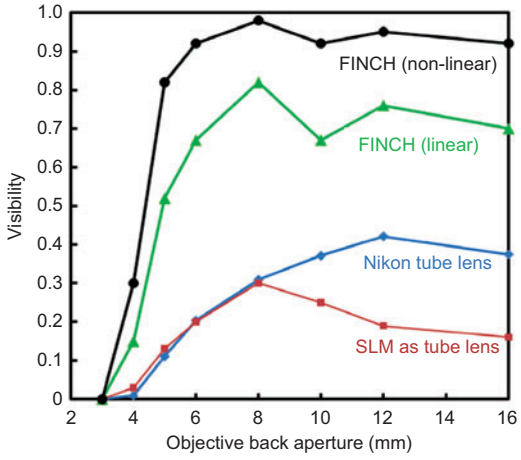

Figure 16 The visibility of the three smallest features of the USAF test pattern in three imaging modes as a function of the size of the aperture placed on the back plane of the objective. Data with the tube lens were taken with the lens and camera configured for standard fluorescence microscopy. Data for the SLM as the tube lens or with the FINCH method (z-ratio=1.8) were taken at a SLM camera distance of 1380 mm. Data for the FINCH images are shown for both linear and non-linear reconstructions.

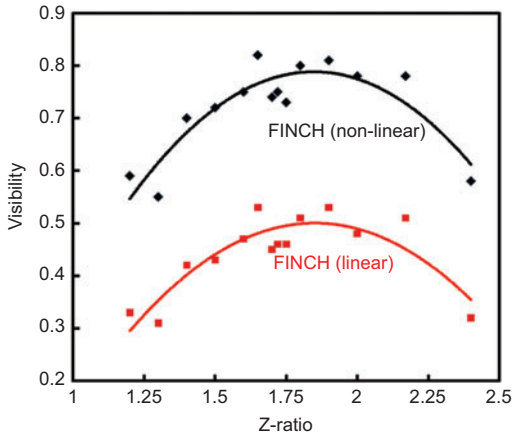

Figure 17 Plots of the visibility of the three smallest USAF features in FINCH as a function of the z-ratio, taken with a 5-mm aperture in the back plane of the objective. Data for both linear and non-linear reconstructions are shown. These data were taken with a z_h of 1380 mm. For comparison, the visibility in standard microscopy is approximately 0.1 when the aperture is 5 mm (see Figure 16).

8-m curvature of the SLM) and the maximum resolution is obtained at approximately z_h/f_d=1.8. Note that although the focal length of the diffractive lens displayed on the SLM is corrected to account for the inherent curvature of the SLM, the constant phase mask cannot be corrected, and therefore the model shown in Figure 13C is valid here.

8. Discussion and conclusions

We have reviewed a new method of generating incoherent digital Fresnel holograms. The reviewed hologram, FINCH, is actually recorded by an on-axis, single-channel, incoherent interferometer. This method inherently does not scan the object in either space or in time. Therefore, FINCH can generate the holograms rapidly without sacrificing the system resolution. FINCH offers the feature of observing a complete volume from a hologram, potentially enabling objects moving quickly in three dimensions to be tracked. The FINCH technique shows great promise in rapidly recording 3D information in any scene, independently of the illumination. In addition, we have described a rapid, non-scanning holographic fluorescence microscope that produces in-focus images at each plane in the specimen from holograms captured on a digital camera. This motionless 3D microscopy technique does not require complicated alignment or a laser. The fluorescence emission can be of relatively wide bandwidth because the optical path difference between the beams is minimal in this single-path device. Although at present each reconstructed section is not completely confocal, 3D reconstructions free of blur could be created by deconvolution of the holographic sections as is typically carried out in widefield microscopy. Time resolution is currently reduced because three holograms need to be captured sequentially. However, in the future, it will be possible to record the three holograms faster using more sensitive cameras, simultaneously capture all three holograms, or to overcome the holographic twin image problem and capture only one hologram, as any of the three holograms contain all the essential 3D information. In the present studies, the image sections were obtained by a process of first capturing three holograms, computing the image z sections from the complex hologram and then, in some cases, further enhancing them by deconvolution. This process could be simplified in the future for real-time display of the holographic image, either with a holographic display system or by algorithms that create the enhanced sections and the 3D representation directly from the single hologram. There is no need for sectioning or scanning or any mechanical movement. Therefore, this system would be expected to be ultimately faster, simpler and more versatile than existing 3D microscopy techniques, which rely on pinhole imaging or deconvolution of stacks of widefield images.

We have also demonstrated fluorescence holography using the high-NA objectives widely used in biological imaging. FINCHSCOPE is able to spatially resolve small beads, biological specimens and different fluorescence emission colors in x, y and z planes with perfect registration. The system provides a simple, flexible, cost-effective and powerful microscopic platform for 3D imaging.

By using the polarization properties of the SLM it is possible to utilize the same pixels to pass both the plane and spherical waves by including input and output polarizers in the system. This has two advantages: (i) the resolution of the lens patterns is increased because all of the SLM pixels can be used to more accurately represent the lens function (the quadratic phase pattern is not interrupted by non-functional pixels). (ii) The plane and spherical wave come from the same pixel and thus the interference is not approximated from adjacent or otherwise random pixels. The configuration used in the present experiments was established to determine the factors necessary for optimal resolution in a FINCH microscopy system. Thus, the configuration is not the most light efficient. For example, the devices used to control polarization are inefficient and reduce the light more than 50%. There is also only 25% efficiency by using the beam splitting cube so that the SLM can be used on axis. Having established the resolution potential of FINCH, it was possible to produce diffractive lens patterns with the SLM positioned at 45°, eliminating the need for the beam splitter, so that most of the light is reflected into the camera and no light loss occurs at this step.

In spite of the inefficiency of the light budget in our configuration, high quality reconstructed images were obtained at very low light levels. The signal-to-noise level in the FINCH system is not very dependent upon the intensity of the hologram being captured but is more dependent upon the extent of interference between the two waves propagating from the SLM. In contrast to what would be expected in conventional imaging, the highest resolution reconstructed images did not come from the holograms with the highest intensity, but rather from the holograms in which the greatest proportion of both plane and spherical waves produced the interference pattern. Thus, in FINCH imaging, obtaining a high degree of interference visibility between the couples of plane and spherical waves is a more critical factor than simply maximizing the intensity of the recorded holograms.

We have analyzed FINCH with the tools of the linear system theory. The theoretical conclusions are well supported by experiments described herein. The main conclusions are:

- FINCH is a hybrid system in the sense that its MTF has the shape of a coherent imaging system, but in the optimal conditions its spatial bandwidth is equal to that of an incoherent system.
- The width of the PSF of FINCH, and accordingly its resolution, is dependent on its configuration and on the ratio between the distance from the SLM to the camera and the focal length of the diffractive lens. In all the possible configurations, the condition to obtain maximum resolution occurs when there is a perfect overlap between the projections of the two different interfering beams (originating from the same point source) on the camera sensing plane.
- Under the optimal condition described in above, FINCH can resolve better than a regular glass lenses-based imaging system with the same numerical aperture. In terms of Rayleigh criterion the improvement is between 1.5- and 2-fold in comparison to incoherent and coherent systems, respectively.

The experimental data very well supports our theoretical predictions. First, we have shown that indeed the resolution of FINCH at the focal plane is better than that of a regular microscope with the same numerical aperture. The native microscope objective yielded better resolution with FINCH than with standard imaging. Furthermore, reduction in the back aperture over a wide range shown in Figure 16 enabled us to demonstrate significantly greater resolution with FINCH compared to standard microscope imaging. Moreover, as the aperture size decreased, the graph of the visibility drops much more steeply in the case of FINCH than in the case of the glass tube lens, indicating that its MTF is more uniform in the range below the cut-off frequency. Because FINCH resolution at the focal plane exceeds standard imaging methods, a natural outcome of our present experiments will be to extend the theoretical analysis and experimental verification to 3D objects which by standard imaging methods are out of focus above and below the focal plane but are resolved by FINCH. In the second experiment, we verify the relationship between resolution and the ratio z_h/f_d. As predicted theoretically, the curve of visibility versus z_h/f_d is not flat but has a maximum value not far from the predicted ratio $z_h/f_d=2$.

Other aspects of FINCH, out of scope of this review, have been published in Refs. [24–27]. These studies include noise suppression by FINCH [24], super-resolution achieved by FINCH in a synthetic aperture mode [25, 26] and the axial resolution which can be achieved by FINCH [27]. The theoretical and experimental data presented here and in Refs. [17–27] make FINCH an attractive platform for a very simple super-resolution 3D imaging system that can resolve better than any conventional imaging system with the same numerical aperture.

Acknowledgments

Part of the work reviewed herein was done in collaboration with N. Siegel. This work was supported by The Israel Ministry of Science and Technology (MOST) to J.R. and by NIST ARRA Award No. 60NANB10D008 to G.B. and by Celloptic, Inc.

Author contributions

All authors contributed equally to this work.

References

[1] G. W. Stroke and R. C. Restrick III, Appl. Phys. Lett. 7, 229–231 (1965).
[2] J. B. Breckinridge, Appl. Opt. 13, 2760–2762 (1974).
[3] A. W. Lohmann, J. Opt. Soc. Am. 55, 1555–1556 (1965).
[4] G. Cochran, J. Opt. Soc. Am. 56, 1513–1517 (1966).
[5] A. S. Marathay, J. Opt. Soc. Am. A4, 1861–1868 (1987).
[6] L. M. Mugnier, G. Y. Sirat, and D. Charlot, Opt. Lett. 18, 66–68 (1993).
[7] G. Pedrini, H. Li, A. Faridian, and W. Osten, Opt. Lett. 37, 713–715 (2012).
[8] Y. Li, D. Abookasis, and J. Rosen, Appl. Opt. 40, 2864–2870 (2001).
[9] Y. Sando, M. Itoh, and T. Yatagai, Opt. Lett. 28, 2518–2520 (2003).
[10] N. T. Shaked and J. Rosen, J. Opt. Soc. Am. A25, 2129–2138 (2008).
[11] J.-H. Park, M.-S. Kim, G. Baasantseren, and N. Kim, Opt. Express 17, 6320–6334 (2009).
[12] T.-C. Poon and A. Korpel, Opt. Lett. 4, 317–319 (1979).
[13] B. W. Schilling, T.-C. Poon, G. Indebetouw, B. Storrie, K. Shinoda, et al., Opt. Lett. 22, 1506–1508 (1997).
[14] T.-C. Poon, J. Holography Speckle 1, 6–25 (2004).
[15] J. Rosen, G. Indebetouw, and G. Brooker, Opt. Express 14, 4280–4285 (2006).
[16] T.-C. Poon, in: 'Optical Scanning Holography with MATLAB' (Springer, New York, 2007).
[17] J. Rosen and G. Brooker, Opt. Lett. 32, 912–914 (2007).
[18] J. Rosen and G. Brooker, Opt. Express 15, 2244–2250 (2007).
[19] J. Rosen and G. Brooker, Nat. Photonics 2, 190–195 (2008).
[20] G. Brooker, N. Siegel, V. Wang, and J. Rosen, Opt. Express 19, 5047–5062 (2011).
[21] J. Rosen, N. Siegel, and G. Brooker, Opt. Express 19, 26249–26268 (2011).
[22] B. Katz, J. Rosen, R. Kelner, and G. Brooker, Opt. Express 20, 9109–9121 (2012).
[23] J. W. Goodman, in: 'Introduction to Fourier Optics', 2nd edition (McGraw-Hill, New York, 1996).
[24] B. Katz, D. Wulich, and J. Rosen, Appl. Opt. 49, 5757–5763 (2010).
[25] B. Katz and J. Rosen, Opt. Express 18, 962–972 (2010).
[26] B. Katz and J. Rosen, Opt. Express 19, 4924–4936 (2011).
[27] P. Bouchal, J. Kapitán, R. Chmelík, and Z. Bouchal, Opt. Express 19, 15603–15620 (2011).

Joseph Rosen is the Benjamin H. Swig Professor of Optoelectronics at the Department of Electrical and Computer Engineering, Ben-Gurion University of the Negev, Israel. He received his BSc, MSc, and DSc degrees in electrical engineering from the Technion-Israel Institute of Technology in 1984, 1987, and 1992, respectively. He is a Fellow of the Optical Society of America (OSA) and SPIE (The International Society for Optical Engineering). His research interests include holography, image processing, optical microscopy, diffractive optics, interferometry, biomedical optics, pattern recognition, optical computing and statistical optics. He has coauthored more than 200 scientific journal papers, book chapters and conference publications.

Gary Brooker is Research Professor of Biomedical Engineering at Johns Hopkins University in Baltimore, MD, USA and Director of the Johns Hopkins University Microscopy Center at the Montgomery County Campus of the University. He obtained his PhD in Pharmacology in 1968 at the University of Southern California. Since his PhD, Dr. Brooker was Professor of Pharmacology at the University of Virginia, Professor and Chairman of Biochemistry and Molecular Biology at Georgetown University in Washington, DC and has been at Johns Hopkins University since 1998. He is a Fellow of the Optical Society of America (OSA). Dr. Brooker's research interests in molecular mechanisms of cardiac contraction, hormone desensitization and cancer cell resistance to chemotherapeutic agents led to his interests and developments in microscope optics. He also founded Atto Bioscience (now acquired by Becton-Dickinson & Co.), which developed and marketed a number of products such as the CARV white light spinning disk confocal microscope and the AttoArc variable intensity microscope arc light source in partnership with Carl Zeiss. His current interests are in developing non-scanning holography and widefield 2-photon microscopy for fast and simple 3D fluorescence microscopy. He has coauthored more than 200 scientific journal papers, book chapters and conference publications.